Inorganic Chemistry

Article

pubs.acs.org/IC

Homologous Series of Layered Perovskites $A_{n+1}B_nO_{3n-1}Cl$: Crystal and Magnetic Structure of a New Oxychloride $Pb_4BiFe_4O_{11}Cl$

Maria Batuk,*[,†] Dmitry Batuk,[†] Alexander A. Tsirlin,[‡,§] Marina G. Rozova,[⊥] Evgeny V. Antipov,[⊥] Joke Hadermann,[†] and Gustaaf Van Tendeloo[†]

[†]Electron Microscopy for Materials Research (EMAT), University of Antwerp, Groenenborgerlaan 171, B-2020 Antwerp, Belgium

[‡]National Institute of Chemical Physics and Biophysics, 12618 Tallinn, Estonia

[§]Max Planck Institute for Chemical Physics of Solids, Nöthnitzer Strasse 40, 01187 Dresden, Germany

[⊥]Department of Chemistry, Moscow State University, 119992 Moscow, Russia

Supporting Information

ABSTRACT: The nuclear and magnetic structure of a novel oxychloride $Pb_4BiFe_4O_{11}Cl$ has been studied over the temperature range 1.5−700 K using a combination of transmission electron microscopy and synchrotron and neutron powder diffraction [space group *P*4/*mbm*, a = 5.5311(1) Å, c = 19.586(1) Å, T = 300 K]. $Pb_4BiFe_4O_{11}Cl$ is built of truncated $(Pb,Bi)_3Fe_4O_{11}$ quadruple perovskite blocks separated by CsCl-type $(Pb,Bi)_2Cl$ slabs. The perovskite blocks consist of two layers of FeO_6 octahedra located between two layers of FeO_5 tetragonal pyramids. The FeO_6 octahedra rotate about the c axis, resulting in a $\sqrt{2}a_p \times \sqrt{2}a_p \times c$ superstructure. Below T_N = 595(17) K, $Pb_4BiFe_4O_{11}Cl$ adopts a G-type antiferromagnetic structure with the iron magnetic moments confined to the *ab* plane. The ordered magnetic moments at 1.5 K are 3.93(3) and 3.62(4) μ_B on the octahedral and square-pyramidal iron sites, respectively. $Pb_4BiFe_4O_{11}Cl$ can be considered a member of the perovskite-based $A_{n+1}B_nO_{3n-1}Cl$ homologous series (A = Pb/Bi; B = Fe) with n = 4. The formation of a subsequent member of the series with n = 5 is also demonstrated.

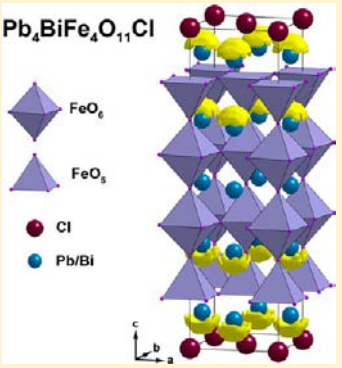

1. INTRODUCTION

$BiFeO_3$ is a unique multiferroic perovskite-type material that exhibits ferroelectric and antiferromagnetic (AFM) ordering well above room temperature (T_C = 1103 K and T_N = 643 K, respectively).[1,2] A structural deformation that triggers ferroelectricity in $BiFeO_3$ is induced by the lone electron pair on the Bi^{3+} cation.[3,4] The electronic structure of Pb^{2+} is similar to that of Bi^{3+}: they both have a lone electron pair, which might cause polar distortions of the crystal structure. Therefore, lead-containing ferrites are a promising playground for searching new multiferroics, and a number of attempts to synthesize such compounds have been made. However, the distorted perovskite $PbFeO_3$ was only obtained under a high pressure of 7 GPa.[5] The Fe cations in $PbFeO_3$ retain their oxidation state 3+, whereas the Pb cations adopt the oxidation states 2+ and 4+. This exemplifies why such a perovskite hardly exists at ambient conditions: the hypothetical "$Pb^{2+}Fe^{4+}O_3$" compound is unstable with respect to the internal oxidation of Pb^{2+} toward Pb^{4+} with the ensuing reduction of Fe^{4+} to Fe^{3+}. Moreover, the Pb^{4+} cation is definitely too small for the 12-coordinated cavity of the perovskite framework.

Perovskite-type lead ferrites combining Pb^{2+} and Fe^{3+} can be formed in two ways. The first approach consists of the reduction of the oxygen content in the structure. When the synthesis temperature is below 700 °C, an anion-deficient partially disordered "$Pb_2Fe_2O_5$" intergrowth structure is formed.[6] At higher temperatures, the oxygen deficiency is accommodated through the periodic arrangement of translational interfaces, similar to crystallographic shear planes.[7,8] Another approach implies a heterovalent substitution in the anion sublattice, reducing its overall charge. Halide ions can be used for this purpose because they have a twice-smaller negative charge than oxygen. The heterovalent replacement of oxygen by fluorine was successful only under high pressure, which enables the formation of $Pb^{2+}Fe^{3+}O_2F$.[9,10] At room temperature, $PbFeO_2F$ has a cubic perovskite structure with a random off-center displacement of the Pb atoms along the symmetrically equivalent ⟨110⟩ directions.

The introduction of larger Cl^- or Br^- anions into the Pb−Fe−O system yields the crystal structure of the mineral hematophanite $Pb_4Fe_3O_8Cl$.[11−14] Hematophanite and its bromine analogue $Pb_4Fe_3O_8Br$ are built of incomplete perovskite $Pb_4Fe_3O_8$ blocks separated by a layer of Cl or Br atoms. Every perovskite block consists of a corner-sharing FeO_6 octahedral layer that is on both sides connected to the sheets of FeO_5 square pyramids, thus forming a slab with a thickness of $2a_p$, where a_p is the lattice parameter of the perovskite subcell.

In this contribution, we establish a novel perovskite-related $A_{n+1}B_nO_{3n-1}Cl$ (A = Pb/Bi; B = Fe) homologous series based upon the expansion of the perovskite blocks in the hematophanite structure. We report the crystal and magnetic

Received: December 6, 2012
Published: February 5, 2013

   dx.doi.org/10.1021/ic302667a | *Inorg. Chem.* 2013, 52, 2208−2218

structure of the $n = 4$ member $Pb_4BiFe_4O_{11}Cl$ and the existence of a higher ($n = 5$) member of the series.

2. EXPERIMENTAL SECTION

Samples of $Pb_4BiFe_4O_{11}Cl$ were synthesized by a solid-state reaction of PbO, $PbCl_2$, Bi_2O_3, and Fe_2O_3 in sealed silica tubes. The starting materials were weighed, thoroughly ground, and pressed into pellets, which were then put into aluminum crucibles and sealed in quartz ampules under a dynamical vacuum of 10^{-4} mbar. The samples were annealed in three steps: the preliminary calcination at 700 °C for 3 h was followed by two annealing stages at 800 °C for 8 h. After each intermediate annealing, the samples were reground, pelletized, and sealed again into the silica ampules. Because of the high volatility of lead oxide, a phase-pure sample of $Pb_4BiFe_4O_{11}Cl$ could be obtained only when a 5 mol % excess of PbO was used. Apart from $Pb_4BiFe_4O_{11}Cl$ ($n = 4$ member of the $A_{n+1}B_nO_{3n-1}Cl$ series), the synthesis of higher homologues was attempted. The preparation of two successive members with $n = 5$ ($Pb_4Bi_2Fe_5O_{14}Cl$) and $n = 6$ ($Pb_4Bi_3Fe_6O_{17}Cl$) was endeavored under the same synthesis conditions.

The phase purity of the samples was verified using powder X-ray diffraction (PXRD) data recorded on a Huber G670 Guinier diffractometer [Cu $K\alpha_1$ radiation, curved Ge(111) monochromator, transmission mode, image plate]. The chemical composition was confirmed by energy-dispersive X-ray (EDX) analysis, which was conducted on a JEOL 5510 scanning electron microscope equipped with an INCAx-sight 6587 system (Oxford Instruments). The EDX spectra from about 50 crystallites were collected, and the Pb−M, Bi−M, Cl−K, and Fe−K lines were used to determine the elemental ratio.

The crystal structure of $Pb_4BiFe_4O_{11}Cl$ was investigated by a combination of synchrotron and neutron powder diffraction data and transmission electron microscopy (TEM).

High-resolution synchrotron powder X-ray diffraction (SXPD) data were collected at the ID31 Beamline of European Synchrotron Radiation Facility (ESRF, Grenoble, France) at wavelength 0.3542 Å in the 2θ range 0−30°. The powder sample was thoroughly ground and placed in a thin-walled borosilicate glass capillary with a diameter of ∼0.3 mm. It was spun during the experiment. The SXPD patterns were recorded at 80 and 300 K. The temperature of the sample was controlled by a liquid-nitrogen cryostream.

Neutron powder diffraction (NPD) data were collected on the high-resolution powder diffractometer HRPT at the Laboratory for Neutron Scattering of the Paul Scherrer Institute (LNS PSI, Villigen, Switzerland). The data were collected at wavelength 1.8857 Å in the 2θ range 8−160°. The sample (∼9 g) was placed in a vanadium container with a diameter of 8 mm. The measurements were conducted in the temperature range from 1.5 to 800 K with a step of 50 K. The data from 1.5 to 300 K have been obtained using an ILL ^{4}He flow cryostat. High-temperature measurements were performed using a custom-built tantalum radiation furnace. The crystal and magnetic structures were refined by the Rietveld method in the *JANA2006* package.[15]

Electron diffraction (ED) patterns and high-angle annular dark-field scanning transmission electron microscopy (HAADF-STEM) images were acquired using an FEI Tecnai G^2 (200 kV) electron microscope. Some of the HAADF-STEM images and the annular bright-field STEM (ABF-STEM) images were acquired using an FEI Titan 50-80 microscope operated at 300 kV. The simulated HAADF-STEM and ABF-STEM images were calculated using *QSTEM 2.0* software.[16] The ED investigation of the structural behavior upon heating to 700 K was conducted using a dedicated Gatan heating holder. Samples for the TEM study were prepared by grinding the material under ethanol and depositing a few drops of the suspension onto holey carbon grids. The calculated ED patterns were obtained using *JEMS* software.

The magnetic susceptibility of $Pb_4BiFe_4O_{11}Cl$ was measured using the Quantum Design PPMS equipped with the vibrating sample magnetometer (VSM) option and the high-temperature (oven) insert. The measurements were performed in the temperature range 2−700 K in magnetic fields of up to 5 T in high-vacuum atmosphere (pressure below 10^{-4} mbar).

Electronic structure calculations were performed in the framework of the density functional theory (DFT) using the *FPLO*[17] and *TB-LMTO-ASA* codes[18] and the Perdew−Wang parametrization of the exchange-correlation potential.[19] The reciprocal space was sampled by fine meshes with up to 144 k-points in the symmetry-irreducible part of the first Brillouine zone. An ordered crystal structure with Bi atoms fully occupying the Pb3 position was considered. The effects of strong electronic correlations were taken into account via the mean-field DFT+U procedure with the on-site Coulomb repulsion $U_d = 7$ eV and Hund's exchange $J_d = 1$ eV.[20] The resulting energy spectrum is shown in Figure S4 in the Supporting Information. We have found the energy gap of about 1.6 eV to be in reasonable agreement with the brown color of $Pb_4BiFe_4O_{11}Cl$. The electron localization function (ELF) was obtained from the self-consistent electronic density by an internal numerical procedure of the *TB-LMTO-ASA* program.

3. RESULTS

3.1. Crystal Structure of $Pb_4BiFe_4O_{11}Cl$. According to the EDX data, the compound under investigation has a composition $Pb_{4.0(2)}Bi_{0.9(1)}Fe_{4.1(3)}O_xCl_{1.1(2)}$, which fits within experimental error to the nominal composition $Pb_4BiFe_4O_{11}Cl$. The most intense peaks on the SXPD patterns of $Pb_4BiFe_4O_{11}Cl$ are attributed to the basic perovskite cell with $a_p \approx 3.91$ Å. The entire SXPD pattern can be indexed on a tetragonal lattice with cell parameters $a = 3.91404(4)$ Å $\approx a_p$ and $c = 19.5742(4)$ Å $\approx 5a_p$ and space group $P4/mmm$ (see Figure S1 in the Supporting Information). Because the $c/a = 5.001$ ratio is very close to the integer value, most reflections belong to the pseudocubic basic perovskite cell, and the tetragonal reflection splitting cannot be seen even in the high-resolution SXPD pattern.

The most significant ED patterns of $Pb_4BiFe_4O_{11}Cl$ are shown in Figure 1. The brighter reflections can be indexed with the tetragonal unit cell, as determined from the SXPD data. However, lines of a modulated intensity are observed propagating along the c^* direction (marked with arrows in Figure 1), which indicates an extra ordering in the $Pb_4BiFe_4O_{11}Cl$ structure. A close inspection of the lines reveals that they are not continuous but consist of closely positioned spots. The brighter superlattice reflections in the lines can be indexed by assuming a tetragonal supercell of a twice-larger volume with lattice parameters $\sqrt{2}a_p \times \sqrt{2}a_p \times 5a_p$. This indexation is shown in Figure 1. The superlattice reflections are absent on the ED pattern of the [100] zone, which suggests the following reflection condition $0kl$: $k = 2n$. This leads to the extinction symbol P-b- and possible space groups $P4bm$, $P\bar{4}b2$, and $P4/mbm$. Weak reflections on the [001] ED pattern violating the $0k0$: $k = 2n$ extinction condition are caused by the double diffraction.

Analysis of the modulated intensity arrays reveals a specific distribution of the diffracted intensity over the reflections. Figure 2 shows the intensity profile of the array located around the $\bar{1}20$ reflection. The profile was empirically fitted with a set of Gaussian functions using the software *Fityk*.[21] The position of all reflections can be described in the framework of incommensurate crystallography.[22] In this approach, the reflections indexed on the $\sqrt{2}a_p \times \sqrt{2}a_p \times 5a_p$ cell would be considered as basic reflections and the weak reflections in the arrays as satellites. The position of the satellite reflections can be described by introducing a fourth basic vector $\mathbf{q} = \gamma\mathbf{c}^*$. The complete indexation of the ED pattern can be done using four indexes: $hklm$. Using the intensity profile (see Figure 2),

dx.doi.org/10.1021/ic302667a | *Inorg. Chem.* 2013, 52, 2208−2218

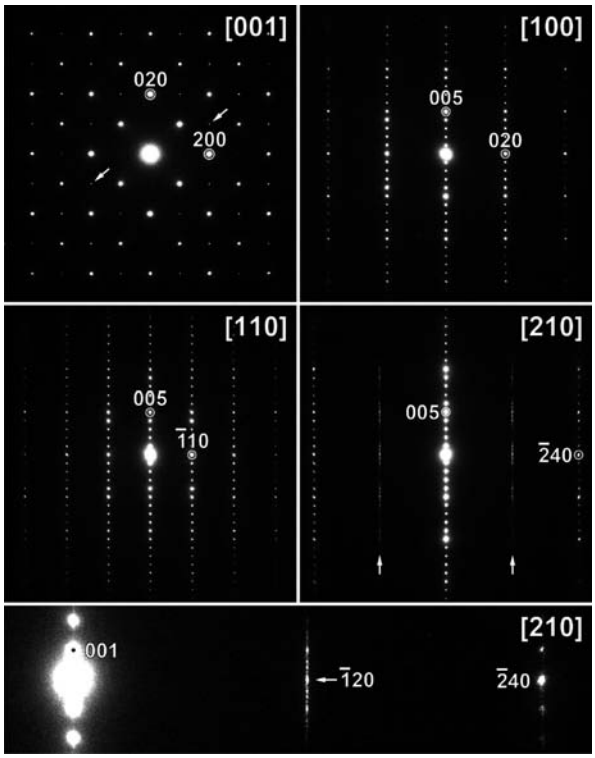

Figure 1. ED patterns of $Pb_4BiFe_4O_{11}Cl$. The patterns are indexed in the $\sqrt{2}a_p \times \sqrt{2}a_p \times 5a_p$ tetragonal supercell.

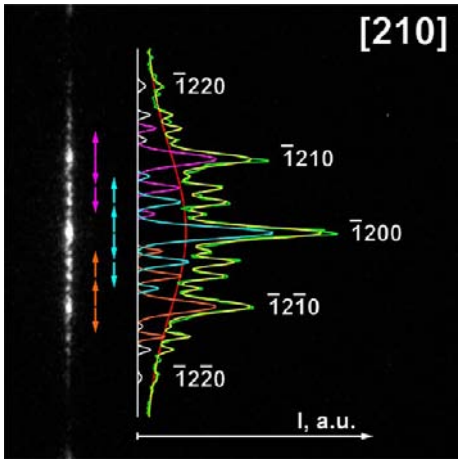

Figure 2. Satellite reflection arrays taken around the position of the $\bar{1}200$ reflection together with the corresponding intensity profile (I). On the plot: the green curve is the experimental profile, yellow is the fitted model, and red is the background. Three brighter basic reflections ($\bar{1}210$, $\bar{1}200$, and $\bar{1}2\bar{1}0$) along with the corresponding satellites of first (m = 1) and second (m = 2) order are shown in different colors (magenta, cyan, and orange, respectively). The positions of the satellite reflections are indicated by arrows of the same color. The weaker reflections (basic $\bar{1}220$, $\bar{1}2\bar{2}0$, and their satellites) are shown in white.

the component of the modulation vector was estimated as $\gamma \approx 0.39$.

The contribution of the modulated intensity arrays to the NPD data is insignificant, and therefore only the average structure with the $\sqrt{2}a_p \times \sqrt{2}a_p \times 5a_p$ cell and centrosymmetric space group $P4/mbm$ has been considered during the refinement. The origin of the structure modulation, which causes satellite reflections on the ED patterns, will be discussed further in the paper.

The cation arrangement in the $Pb_4BiFe_4O_{11}Cl$ structure can be determined directly from the high-resolution HAADF-STEM images. The intensity of the spots on these images depends on the average atomic number Z of the projected columns and scales approximately as Z^n ($1.6 < n < 1.9$). Figure 3 shows the HAADF-STEM image of $Pb_4BiFe_4O_{11}Cl$ taken

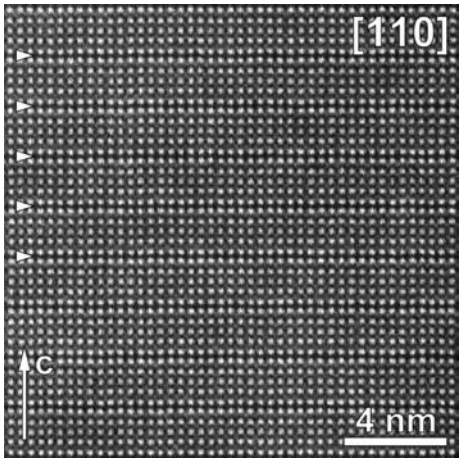

Figure 3. HAADF-STEM image of $Pb_4BiFe_4O_{11}Cl$ taken along the [110] zone axis. Arrowheads indicate the chlorine layers.

along the [110] zone axis, which is the most informative one. The brighter dots are attributed to the Pb/Bi columns (Z_{Pb} = 82; Z_{Bi} = 83). They form a square pattern with a spacing of ≈3.9 Å and correspond to the A positions of the perovskite structure. The Fe−O (Z_{Fe} = 26; Z_O = 8) columns are seen as very weak dots. An ordered alternation of four FeO_2 layers and one chlorine layer along the c axis is seen by the periodic appearance of dark stripes attributed to the chlorine layers (Z_{Cl} = 17; marked by arrowheads in Figure 3). Therefore, the HAADF-STEM image confirms that the structure of $Pb_4BiFe_4O_{11}Cl$ is similar to that of hematophanite $Pb_4Fe_3O_8Cl$.[13,14] They differ only by the thickness of the perovskite blocks confined between the chlorine layers.

A structural model of $Pb_4BiFe_4O_{11}Cl$ can be derived from the parent hematophanite structure by inserting extra FeO_2 and (Pb,Bi)O layers into the perovskite blocks. Thus, the structure is composed of incomplete $(Pb,Bi)_3Fe_4O_{11}$ perovskite blocks separated by the CsCl-type $(Pb,Bi)_2Cl$ slabs. In the perovskite blocks, double layers of corner-sharing FeO_6 octahedra are on both sides connected to sheets of FeO_5 square pyramids through the apical O atoms. Possible atomic displacements that could be responsible for the $\sqrt{2}a_p \times \sqrt{2}a_p \times 5a_p$ superstructure observed on the ED patterns were analyzed with the *ISODISTORT* program.[23] The only distortion compatible with the $P4/mmm$ ($a_p \times a_p \times 5a_p$) → $P4/mbm$ ($\sqrt{2}a_p \times \sqrt{2}a_p \times 5a_p$) transformation is a rotation of the FeO_6 octahedra and FeO_5 pyramids in the perovskite blocks about the c axis. The rotation is restricted by the space symmetry in such a way that both FeO_6 octahedra and both FeO_5 pyramids rotate in phase. However, the rotations of the octahedra and pyramids are independent from each other.

The crystal structure of $Pb_4BiFe_4O_{11}Cl$ was refined by the Rietveld method using the NPD data collected in the temperature range from 1.5 to 700 K. Below 600 K, the material is antiferromagnetically ordered. Corresponding

dx.doi.org/10.1021/ic302667a | *Inorg. Chem.* 2013, 52, 2208−2218

magnetic reflections appear on the NPD patterns, and their intensity systematically grows upon cooling. According to the SXPD and ED data, there are no structural phase transitions in the entire range of thermal stability of the compound. The in situ heating ED investigation demonstrated that even the modulated intensity arrays are persevered up to 700 K, when the material starts to decompose in the vacuum environment of the microscope (see Figure S2 in the Supporting Information). Therefore, the $\sqrt{2}a_p \times \sqrt{2}a_p \times 5a_p$ lattice with space group $P4/mbm$ is sufficient to describe the average structure of the material in the whole temperature range.

In the structural model of $Pb_4BiFe_4O_{11}Cl$, the O1 and O2 atoms form the basal square plane of the FeO_5 pyramids and FeO_6 octahedra, respectively. The displacements of these O atoms in the *ab* plane result in the rotation of the Fe−O polyhedra about the *c* axis. If the rotations are not taken into account, the refinement of the atomic displacement parameters (ADPs) yields a high ADP for the O2 position [U = 0.047(1) Å^2 at 700 K], whereas the ADP of the O1 atom retains a reasonable value of 0.018(1) Å^2. This indicates that the FeO_5 pyramids are only slightly rotated, while the FeO_6 octahedra undergo sizable rotations.

The translational symmetry of the structure implies that all perovskite blocks have the same rotation pattern. However, the satellite reflection arrays appearing on the ED patterns indicate that this translational symmetry is violated, while the long-range periodicity of the Fe−O polyhedral rotation is preserved. This violation is not random and corresponds to the modulation vector **q**. Unfortunately, it cannot be quantitatively described because of the very low intensity of the satellite reflections on the NPD patterns. Nevertheless, one can assume that the structure modulation is caused by the formation of a specific sequence of unit cells with different rotation directions of the octahedra. Two possibilities can be considered. The first one is the periodic occurrence of the cells with FeO_6 octahedra rotated antiphase in the matrix of the cells with in-phase rotation. Another one is alternation of the cells with the octahedra rotated in phase but in opposite directions (clockwise and counterclockwise). Both cases lead to only minor changes in the local coordination environment and, therefore, should not significantly affect the free energy.

To introduce modulation of the octahedral rotation within the average structure, a partially disordered structural model was considered. The position of the O2 atom was split into $O2_1$ and $O2_2$ positions that correspond to the rotation of the $Fe2O_6$ octahedra by the same angle but in the opposite directions. The *x* and *y* coordinates of these atoms were restricted with appropriate linear constraints (see Table 2). The occupancy factors of the $O2_1$ and $O2_2$ positions were refined in the entire temperature range and in every point converged to the values 0.79(2) and 0.21(2). The partially disordered model of the octahedral rotation reduced the thermal parameters of the O2 atoms.

The Pb and Bi atoms jointly occupy the A positions of the perovskite blocks. Because of the very similar neutron scattering lengths of these elements (9.40 fm for Pb; 8.53 fm for Bi), their occupancies could not be accurately refined, and therefore a random distribution of Bi and Pb atoms was adopted. The parameters of the Rietveld refinement at 1.5, 300, and 700 K are listed in Table 1. The fractional atomic coordinates and the ADP values are provided in Table 2 and the selected bond lengths in Table 3. The experimental, calculated, and difference NPD profiles after refinements at 1.5, 300, and 700 K are given in Figure 4. The refined room-temperature crystal structure is shown in Figure 5a.

Table 1. Selected Parameters of the Rietveld Refinements for $Pb_4BiFe_4O_{11}Cl$

formula	$Pb_4BiFe_4O_{11}Cl$		
space group	$P4/mbm$		
T, K	1.5	300	700
a, Å	5.5185(1)	5.5310(1)	5.5629(1)
c, Å	19.521(1)	19.586(1)	19.726(1)
Z	2	2	2
cell volume, Å^3	594.49(2)	599.18(3)	610.45(3)
calcd density, g/cm^3	8.21(4)	8.16(4)	8.00(5)
M(Fe1), μ_B	3.62(4)	3.01(6)	
M(Fe2), μ_B	3.93(3)	3.50(4)	
radiation	neutron, λ = 1.8857 Å		
parameters refined	22	22	20
R_F, R_P, R_{wP}	0.027, 0.036, 0.047	0.027, 0.035, 0.046	0.026, 0.035, 0.046

The structure solution was validated by the STEM data. Figure 6 shows the HAADF-STEM and ABF-STEM images taken at high magnification. The HAADF-STEM image is shown without any postprocessing, whereas the ABF-STEM image was subjected to low-pass filtering to remove the noise from the scanning. In contrast to HAADF-STEM, ABF-STEM imaging demonstrates an absorptive type of contrast, so that atomic columns appear as dark spots on a white background. Owing to the specific position of the annular detector, ABF-STEM is capable of visualizing light atomic columns (O and Cl) even in the presence of the heavy atoms (Pb and Bi).[24] The simulated images (insets in Figure 6), calculated using the refined $Pb_4BiFe_4O_{11}Cl$ structure for a sample thickness of 12 nm, are in good agreement with the experiment.

3.2. Magnetic Structure of $Pb_4BiFe_4O_{11}Cl$. The magnetic reflections can be indexed on the $\sqrt{2}a_p \times \sqrt{2}a_p \times 5a_p$ tetragonal lattice. Therefore, the magnetic cell parameters are equal to those of the nuclear structure, and the propagation vector is **k** = (0, 0, 0). The magnetic symmetry was analyzed using *ISODISTORT* software.[23] All possible AFM structures were tested in the refinement. The NPD profile can be satisfactorily fitted only with the G-type AFM structure that imposes iron magnetic moments oriented along the *a* axis (magnetic space group $Pb'am$) or the *b* axis (magnetic space group $Pba'm$). Because these two possibilities are indistinguishable, the space group $Pb'am$ was selected for the refinement. The magnetic moments of the two iron sites Fe1 (pyramids) and Fe2 (octahedra) were refined independently. When the moments are directed along the *a* axis, canting of the magnetic moments along the *b* axis is possible. However, the *y* component of both moments converged to zero within the experimental uncertainty in the refinement. The values of the magnetic moments at 1.5 K were refined as 3.62(4) μ_B for Fe1 and 3.93(3) μ_B for Fe2.

The magnetic structure of $Pb_4BiFe_4O_{11}Cl$ visualized with *VESTA* software[25] is presented in Figure 7. The temperature dependence of the ordered magnetic moments on the Fe1 and Fe2 sites is shown in Figure 8. The plots were fitted with empirical function $M = M_0(1 - T/T_N)^\beta$, where M_0 is the magnetic moment at 0 K and T_N is the Néel temperature, and β is the critical exponent. The resulting Néel temperature of 595(17) K is similar to that of hematophanite (602 K[12] or 610(5) K[14]).

dx.doi.org/10.1021/ic302667a | *Inorg. Chem.* 2013, 52, 2208−2218

Table 2. Atomic Parameters for $Pb_4BiFe_4O_{11}Cl$ at 1.5, 300, and 700 K

atom	site	x, y, z		1.5 K	300 K	700 K
Pb1[a]	4f	$^1/_2$, 0, z	U_{iso}, Å^2	0.004(1)	0.012(1)	0.029(1)
			z	0.0945(1)	0.0955(1)	0.0963(2)
Pb2[a]	4f	$^1/_2$, 0, z	U_{iso}, Å^2	0.016(1)	0.022(1)	0.037(1)
			z	0.3063(1)	0.3070(2)	0.3067(2)
Pb3[a]	2c	$^1/_2$, 0, $^1/_2$	U_{iso}, Å^2	0.025(1)	0.031(1)	0.058(2)
Fe1	4e	0, 0, z	U_{iso}, Å^2	0.003(1)	0.010(1)	0.026(1)
			z	0.1924(1)	0.1930(1)	0.1935(2)
Fe2	4e	0, 0, z	U_{iso}, Å^2	0.004(1)	0.006(1)	0.020(1)
			z	0.3992(1)	0.3998(1)	0.4003(2)
Cl	2a	0,0,0	U_{iso}, Å^2	0.002(1)	0.015(1)	0.042(2)
O1	8k	x, x − $^1/_2$, z	U_{iso}, Å^2	0.004(1)	0.011(1)	0.025(1)
			x	0.2521(8)	0.2500(10)	0.2506(11)
			y	−0.2479(8)	−0.2500(10)	−0.2494(11)
			z	0.1622(1)	0.1626(1)	0.1624(2)
$O2_1$[b]	8k	x, x − $^1/_2$, z	U_{iso}, Å^2	0.007(1)	0.008(1)	0.024(1)
			x	0.2127(5)	0.2130(5)	0.2172(7)
			y	−0.2873(5)	−0.2870(5)	−0.2828(7)
			z	0.3896(2)	0.3903(2)	0.3922(2)
			SOF	0.80(1)	0.78(1)	0.81(1)
$O2_2$[b]	8k	x, x − $^1/_2$, z	U_{iso}, Å^2	0.007(1)	0.008(1)	0.024(1)
			x	0.2873(5)	0.2870(5)	0.2828(7)
			y	−0.2127(5)	−0.2130(5)	−0.2172(7)
			z	0.3896(2)	0.3903(2)	0.3922(2)
			SOF	0.20(1)	0.22(1)	0.19(1)
O3	4e	0, 0, z	U_{iso}, Å^2	0.014(1)	0.021(1)	0.038(2)
			z	0.2870(2)	0.2876(2)	0.2879(3)
O4	2b	0, 0, $^1/_2$	U_{iso}, Å^2	0.015(2)	0.016(2)	0.025(2)

[a]Occupancy 0.8Pb + 0.2Bi. [b]$O2_2$ fractional coordinates are ($^1/_2$ − x[$O2_1$], −x[$O2_1$], z[$O2_1$]); U_{iso}[$O2_1$] = U_{iso}[$O2_2$].

Table 3. Selected Interatomic Distances for $Pb_4BiFe_4O_{11}Cl$ at 1.5, 300, and 700 K

bond	1.5 K	300 K	700 K
Pb1−O1×2	2.371(4)	2.356(5)	2.363(6)
Pb1−O1×2	2.344(4)	2.356(5)	2.355(5)
Pb1−Cl×4	3.319(1)	3.339(2)	3.369(2)
Pb2−O2×2	2.322(4)	2.332(4)	2.401(5)
Pb2−O2×2	2.768(3)	2.776(4)	2.793(5)
Pb2−O3×4	2.785(1)	2.792(1)	2.806(1)
Pb3−O2×4	2.722(3)	2.718(4)	2.727(4)
Pb3−O2×4	3.111(3)	3.107(3)	3.077(4)
Pb3−O4×4	2.759(1)	2.766(1)	2.781(1)
Fe1−O1×4	2.039(4)	2.044(5)	2.060(6)
Fe1−O3	1.843(5)	1.853(5)	1.862(6)
Fe2−O2×4	1.982(3)	1.985(3)	1.990(4)
Fe2−O3	2.192(5)	2.196(5)	2.217(6)
Fe2−O4	1.968(2)	1.963(3)	1.966(3)

3.3. Higher Members of the $A_{n+1}B_nO_{3n-1}Cl$ Series.

$Pb_4BiFe_4O_{11}Cl$ can be considered as a member of the $A_{n+1}B_nO_{3n-1}Cl$ perovskite-based homologous series with $n = 4$ (more details on this are given in the Discussion section). The subsequent members with $n = 5$ and 6 would have tentative compositions $Pb_4Bi_2Fe_5O_{14}Cl$ and $Pb_4Bi_3Fe_6O_{17}Cl$, respectively. The preparation of these compounds was attempted, and for $n = 5$, the target compound was obtained. The most intense peaks on the PXRD pattern of the $Pb_4Bi_2Fe_5O_{14}Cl$ sample can be indexed on a tetragonal unit cell with lattice parameters $a = 3.9066(1)$ Å $\approx a_p$ and $c = 23.878(1)$ Å $\approx 6a_p$. The $n = 5$ structure is also confirmed by ED and HAADF-STEM observations. According to the ED data, octahedral rotations are present and lead to superlattice reflection arrays similar to those in $Pb_4BiFe_4O_{11}Cl$ (Figure 9). On the HAADF-STEM image of the $n = 5$ structure (Figure 10), every sixth FeO_2 perovskite layer is replaced by a chlorine layer and appears darker. The HAADF-STEM observations confirm that in this structure the perovskite blocks are larger than those of $Pb_4BiFe_4O_{11}Cl$ by one perovskite unit cell.

Although the existence of the $n = 5$ member is clearly demonstrated, a considerable amount of impurities in the samples available so far hinders a precise structural investigation. The HAADF-STEM images in Figure 11 show the defects that are most commonly observed in the samples. These are intergrowths of various structural blocks. The first type of defect is an intergrowth of the perovskite blocks of different thicknesses. This can be seen as a lamella of $n = 4$ in a matrix of $n = 5$ in Figure 11a. The second type is the intergrowth of the perovskite blocks with structural units that appear on the HAADF-STEM images as double layers of A-cation columns arranged in a chessboard manner (marked by a triple asterisk in Figure 11). These layers are enclosed between the chlorine layers, which connect them to the perovskite blocks (Figure 11a) or to each other (Figure 11b). The sequence and atomic arrangement of the layers resemble the structure of the mineral perite ($PbBiO_2Cl$).[26] It is built of $PbBiO_2$ fluorite slabs separated by chlorine layers, forming a CsCl-like arrangement with the two adjacent Pb/Bi layers. Apparently, the chessboard double layers on the HAADF-STEM images of the $n = 5$ samples have the same composition $PbBiO_2$. The observed defects occur because of a local variation of the composition, which leads to the formation of stable structural blocks. As can

dx.doi.org/10.1021/ic302667a | Inorg. Chem. 2013, 52, 2208−2218

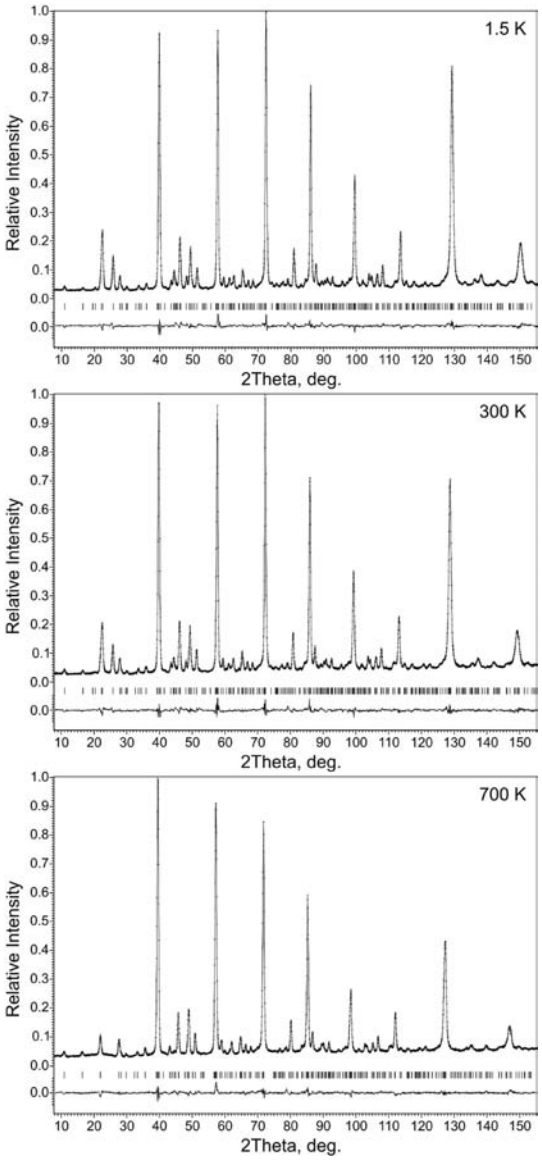

Figure 4. Experimental, calculated, and difference NPD profiles after the Rietveld refinement of the $Pb_4BiFe_4O_{11}Cl$ structure at 1.5, 300, and 700 K.

be seen on the STEM images in Figure 11, they are either perovskite blocks of different thickness or perite slabs. These structural units are bound together by the chlorine layers. Therefore, it is difficult to achieve a homogeneous distribution of the components over the sample. An optimization of the synthesis conditions of the $n = 5$ member is underway and lies outside the scope of the present work. The formation of the $n = 6$ member was not detected at the synthesis conditions used.

3.4. Magnetic Properties. Below room temperature, the magnetic susceptibility of $Pb_4BiFe_4O_{11}Cl$ shows a weak temperature dependence and a more pronounced field dependence (Figure 12) indicative of weak ferromagnetism or trace amounts of a ferromagnetic impurity. The magnetization curve measured at 2 K develops a small hysteresis with a remnant magnetization of $M_r \approx 0.01\ \mu_B$/fu (Figure S3 in the Supporting Information). The measurement above room temperature reveals a marginal change in the slope of the susceptibility curve at 600 K (inset of Figure 12). While this change could be attributed to the AFM ordering observed by

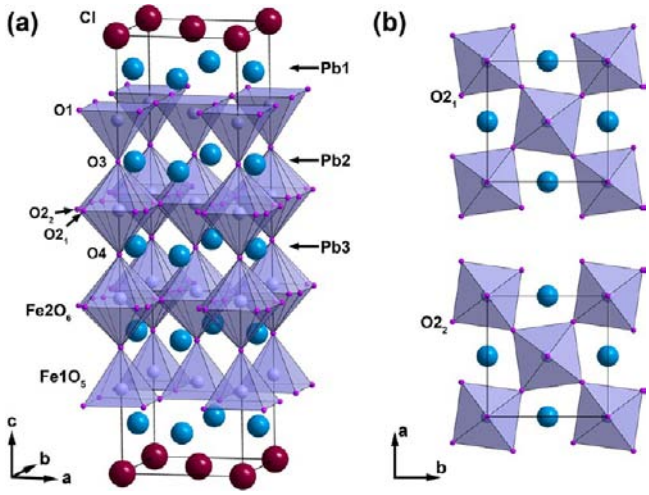

Figure 5. (a) The room-temperature structure of $Pb_4BiFe_4O_{11}Cl$. The O2 positions are split due to the disorder in the rotations of the $Fe2O_6$ octahedra. (b) Top view of the octahedral layers. Each unit cell contains either $O2_1$ or $O2_2$ that correspond to opposite directions of the octahedral rotations.

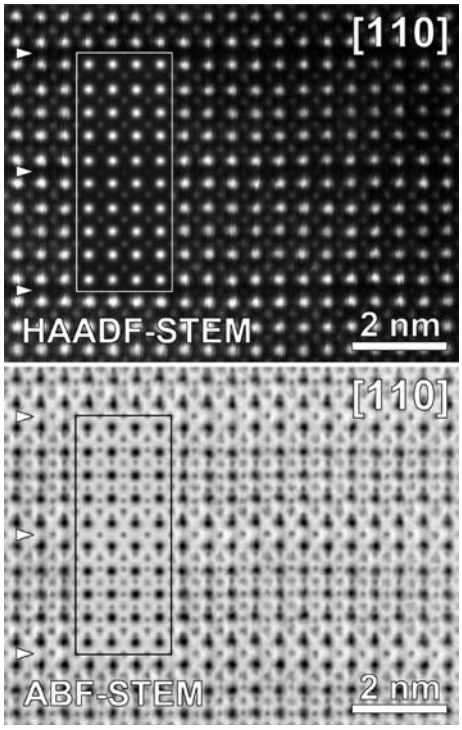

Figure 6. High-magnification HAADF-STEM and ABF-STEM images of $Pb_4BiFe_4O_{11}Cl$ along [110]. The arrowheads indicate the chlorine layers. The insets show simulated images calculated using the structural parameters refined from the NPD data. The HAADF-STEM image is shown as recorded. The noise from the scanning of the ABF-STEM image has been removed by low-pass filtering.

NPD at $T_N = 595(17)$ K, the heating/cooling behavior is irreversible and indicates the onset of sample decomposition upon heating in vacuum. Unfortunately, the poor chemical stability above T_N makes a detailed investigation of the magnetic transition with magnetization measurements impossible in $Pb_4BiFe_4O_{11}Cl$.

The data collected at low temperatures after heating the sample in the oven chamber show the same field dependence as

dx.doi.org/10.1021/ic302667a | Inorg. Chem. 2013, 52, 2208−2218

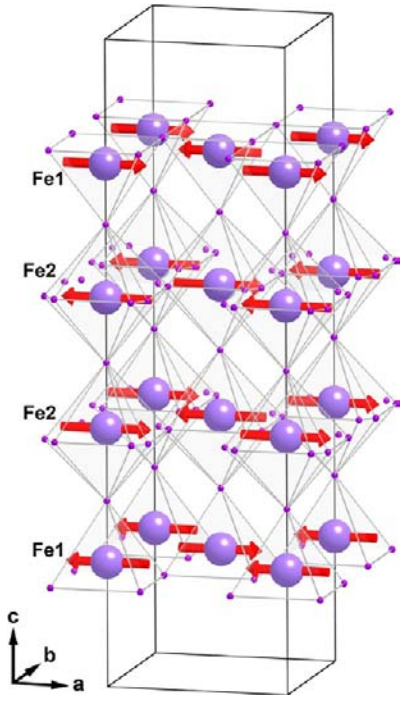

Figure 7. Magnetic structure of $Pb_4BiFe_4O_{11}Cl$ at 1.5 K (Cl, Pb, and Bi atoms are removed for clarity). The Fe1 and Fe2 spins are parallel to the *a* axis.

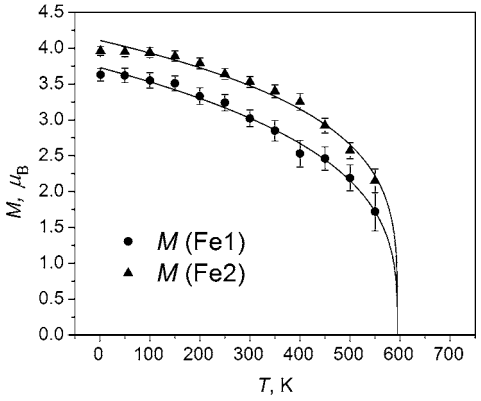

Figure 8. Temperature dependence of ordered magnetic moments for Fe1 and Fe2. The data are fitted with the $M = M_0(1 - T/T_N)^{\beta}$ function. The fitting parameters are T_N = 595(17) K, M_0(Fe1) = 3.73(4) μ_B, M_0(Fe2) = 4.11(4) μ_B, β(Fe1) = 0.30(3), and β(Fe2) = 0.24(1).

the pristine sample. This field dependence is present up to at least 700 K, i.e., well above T_N of $Pb_4BiFe_4O_{11}Cl$. Therefore, one can safely conclude that the weak ferromagnetism of the samples has an extrinsic origin (for example, M_r of 0.01 μ_B/fu can be induced by only 0.2 wt % of a ferromagnetic Fe^{3+}-containing oxide, which is undetectable by powder diffraction techniques). The $Pb_4BiFe_4O_{11}Cl$ itself has no net magnetic moment and likely develops a collinear, noncanted AFM structure, as independently observed by NPD.

4. DISCUSSION

The nuclear structure of $Pb_4BiFe_4O_{11}Cl$ is shown in Figure 5a. There are two types of iron coordination environments in the structure: the Fe1 atom has a 5-fold square-pyramidal coordination, whereas Fe2 has a 6-fold octahedral coordination.

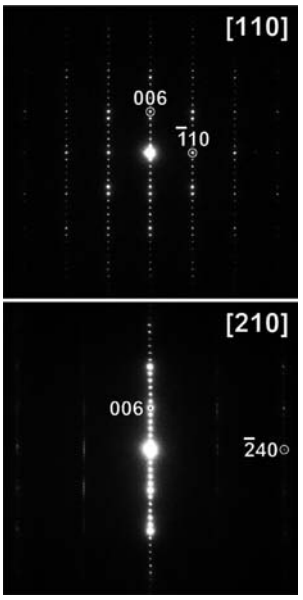

Figure 9. ED patterns of the n = 5 member of the $A_{n+1}B_nO_{3n-1}Cl$ series.

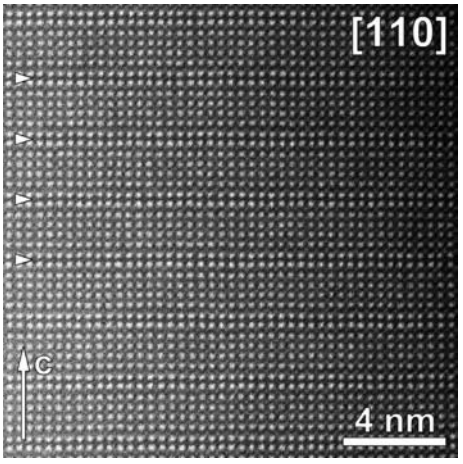

Figure 10. [110] HAADF-STEM image of the n = 5 member of the $A_{n+1}B_nO_{3n-1}Cl$ series. Arrowheads indicate the chlorine layers.

In the $Fe1O_5$ pyramids, the Fe1−O distance is shorter for the apical O3 atom, d(Fe1−O3) = 1.85 Å, and longer for the basal O1 atoms, d(Fe1−O1) = 2.04 Å. A similar distortion of the pyramids is observed in hematophanite $Pb_4Fe_3O_8Cl$, where the apical and equatorial distances are 1.88 and 2.03 Å, respectively.[13,14] The Fe2 atom in the $Fe2O_6$ octahedra is displaced from the basal oxygen plane by 0.1 Å along the *c* axis toward the center of the perovskite block. This displacement results in different distances between Fe2 and the apical O atoms: d(Fe2−O3) = 2.20 Å and d(Fe2−O4) = 1.96 Å. The distance between Fe2 and the basal O2 atom is 1.99 Å. Therefore, Fe2 has an asymmetric coordination with five shorter bonds of comparable length and one bond that is significantly longer.

The bond valence sum (BVS)[27,28] calculated for the iron positions demonstrates a considerable difference in the valence of the octahedral Fe2 (3.05) and pyramidal Fe1 (2.64) sites. Similar BVS values were obtained for the hematophanite structure (3.03 and 2.60 for the octahedral and pyramidal sites, respectively). The BVS value for the Fe1 position indicates

dx.doi.org/10.1021/ic302667a | Inorg. Chem. 2013, 52, 2208−2218

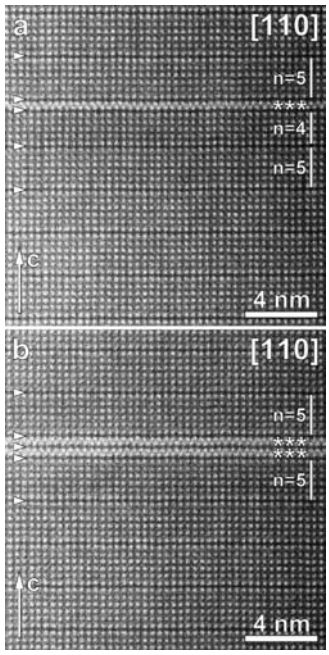

Figure 11. [110] HAADF-STEM image, showing defects observed in the $A_{n+1}B_nO_{3n-1}Cl$ series. Arrowheads indicate the chlorine layers. The $PbBiO_2$ fluorite slabs are marked with a triple asterisk (***).

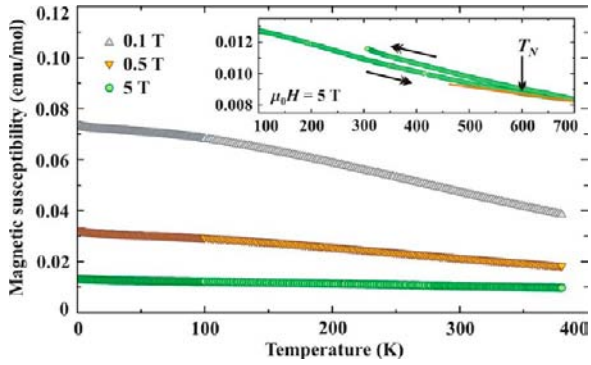

Figure 12. Magnetic susceptibility of $Pb_4BiFe_4O_{11}Cl$ measured in applied fields of 0.1, 0.5, and 5 T. The inset shows a high-temperature measurement in the high-vacuum VSM oven. Note the change in the slope around $T_N \sim 600$ K and the irreversible thermal behavior that indicates the decomposition.

significant underbonding, which can be related to a tensile strain in the vicinity of the CsCl-like $(Pb,Bi)_2Cl$ block. This strain originates from a geometrical mismatch between the $(Pb,Bi)_2Cl$ block and the perovskite slab. The characteristic in-plane dimensions of the $(Pb,Bi)_2Cl$ block can be estimated from the data for the $BiPbO_2Cl$ structure as 3.96 Å.[26] The in-plane dimensions are notably larger than those of the $Pb_4BiFe_4O_{11}Cl$ structure (3.91 Å). This tensile strain should also suppress rotation of the FeO_5 pyramids because lengthening of the basal Fe1−O distances would result in further underbonding of the Fe1 cations. The cooperative rotations of the $Fe2O_6$ octahedra are, nevertheless, necessary to optimize the coordination environment of the Pb3 cations at the center of the perovskite blocks.

At room temperature, the angle of rotation of the $Fe2O_6$ octahedra about the *c* axis is 8.2(2)°. As was discussed in the Results section, the ED data indicate an ordered alternation of cells with different directions of the rotation. This alternation corresponds to the modulation vector $\mathbf{q} \approx 0.39\mathbf{c}^*$. To ascertain the nature of the modulation, an approximation with $\mathbf{q} \approx 2/5\mathbf{c}^*$ was considered, resulting in a 5-fold superstructure along the *c* direction. The ratio between the occupancy factors of the $O2_1$ and $O2_2$ atoms is 0.79(2):0.21(2), which indicates that $^4/_5$ of the octahedra are rotated in one direction (say, A) and $^1/_5$ in the opposite direction (say, B). Considering the 5-fold superstructure, that would mean that 8 out of 10 octahedral layers are rotated in the A direction, while the other 2 are rotated to the same angle but in the B direction. There are two octahedral layers in one unit cell, and thus there are two possible scenarios how these 2 layers with the opposite rotation can be distributed over the 10 octahedral layers in 5 cells. The first one is that there are 2 cells with the antiphase rotation, attributed to the octahedral sequence AB (or BA) and 3 cells with the in-phase AA rotation. The second one corresponds to 1 cell with the BB rotation alternating with 4 cells with the AA rotation. Analysis of the ordered sequences that could possibly be formed in these two cases was done similarly to that described by Perez-Mato et al.[29] employing the Farey series of order. It shows that the second scenario with the BB rotation cell leads to the modulation vector $\mathbf{q} \approx 1/5\mathbf{c}^*$, which is inconsistent with the ED data. The first scenario results in the correct modulation vector. The most probable stacking sequence is following: AB(BA)-AA-AB(BA)-AA-AA. To confirm the results of this analysis, theoretical ED patterns were calculated for every possible distribution of the AB, BA, and BB cells in the matrix of the AA 5-fold superstructure. The comparison of the satellite reflection array from the experimental ED pattern with the theoretical ones is shown in Figure S5 in the Supporting Information. One can notice that the sequences AB−AA−AB−AA−AA and BA−AA−AB−AA−AA best reproduce the intensity distribution over the basic reflections and satellites.

The octahedral rotation also occurs in the structure of hematophanite $Pb_4Fe_3O_8Cl$[14] and its copper analogues $Pb_y(Ba/Sr)_{4-y}Cu_2MO_8X$ (where M = Nb, Ta, Sb, Ru, X = Cl, Br, and $2 \le y \le 3$[30−33]) but in a completely disordered manner, whereas for the $Pb_3(Ba/Sr)_3Cu_3O_8X$ (X = Cl, Br)[34,35] structure, a $\sqrt{2}a_p \times \sqrt{2}a_p \times c$ superlattice was experimentally observed by ED.

Pb^{2+} and Bi^{3+} in the perovskite-based ferrites are prone to an off-center displacement. The mixing of the Pb(Bi) 6s and O 2p states results in a strong covalent A−O bonding that shifts the Pb(Bi) atoms toward a group of O atoms. The remaining A−O distances are elongated, thus creating a cavity that is loosely understood as the "position of the lone pair" and indeed shows signatures of electron localization (high values of the ELF). The displacements of Pb^{2+} and Bi^{3+} can be disordered, as in $PbFeO_2F$[10] and $Bi_{0.81}Pb_{0.19}FeO_{2.905}$,[36] or demonstrate an antipolar ordering, as in the anion-deficient $(Pb,Bi)_{1-x}Fe_{1\pm x}O_{3-y}$ perovskites modulated by crystallographic shear planes.[37] In $Pb_4BiFe_4O_{11}Cl$, such displacements are rather weak, and yet the ELF plot (Figure 13) shows well-defined isosurfaces around the Pb1 and Pb2 positions. The Pb1 atom has four short bonds to O and four very long bonds to Cl, whereas Pb2 has two short and six long Pb−O bonds. The respective displacements are ordered in a ferroelectric manner within each layer (*ab* plane) and in an antiferroelectric manner on opposite sides of the perovskite block (Figure 13). The resulting structure is nonpolar (antiferroelectric). The local environment of Pb3 remains symmetric and features eight Pb−O distances of similar length (2.72−2.76 Å). However, the sizable ADP of Pb3 [U_{iso} = 0.025(1) Å^2 at 1.5 K] is indicative of

dx.doi.org/10.1021/ic302667a | Inorg. Chem. 2013, 52, 2208−2218

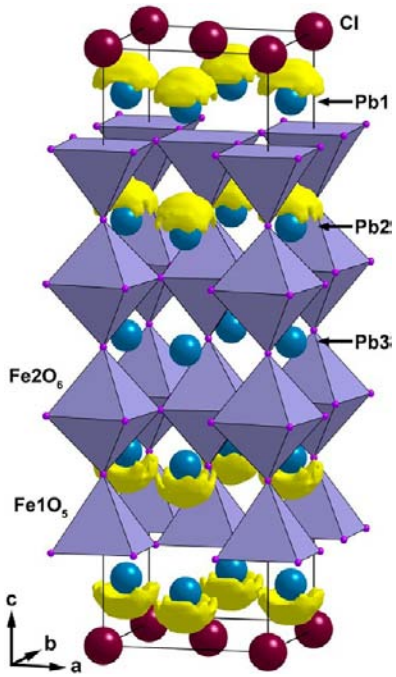

Figure 13. ELF isosurfaces (η = 0.8) for the $Pb_4BiFe_4O_{11}Cl$ structure. The isosurfaces are observed only for the Pb1 and Pb2 atoms with asymmetric local environment.

static local displacements that may also be present for Pb2 [U_{iso} = 0.016(1) Å^2 at 1.5 K].

The temperature evolution of the $Pb_4BiFe_4O_{11}Cl$ structure is very similar to that of hematophanite $Pb_4Fe_3O_8Cl$. Both the *a* and *c* lattice parameters monotonically grow (Figure 14) upon

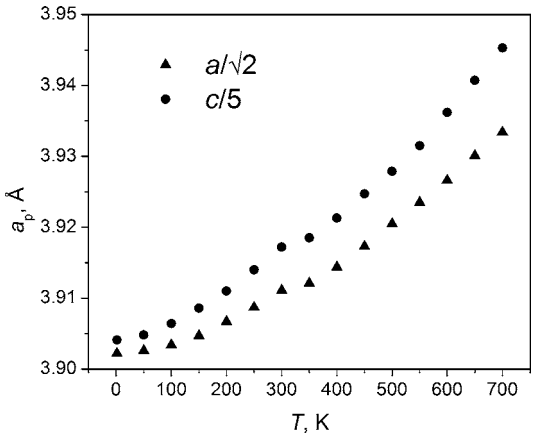

Figure 14. Temperature dependence of the *a* and *c* lattice parameters. The values are normalized to the perovskite subcell. The small kinks at room temperature are due to changes of the sample environment.

heating. In the temperature range 1.5−700 K, the structure almost isotropically expands by ≈0.8% and ≈1.1% in the *a* and *c* directions, respectively. The increase in the *c* cell parameter is mainly related to the expansion of the $(Pb,Bi)_2Cl$ layer. The thickness of this layer can be measured by the Pb1−Pb1 distance. Its temperature evolution is plotted in Figure 15. As can be seen in Table 3, the configuration of the perovskite blocks does not change considerably in the whole temperature range. The angle of the rotation of the octahedra decreases with temperature from 8.4(2)° at 1.5 K to 7.6(2)° at 700 K. In the

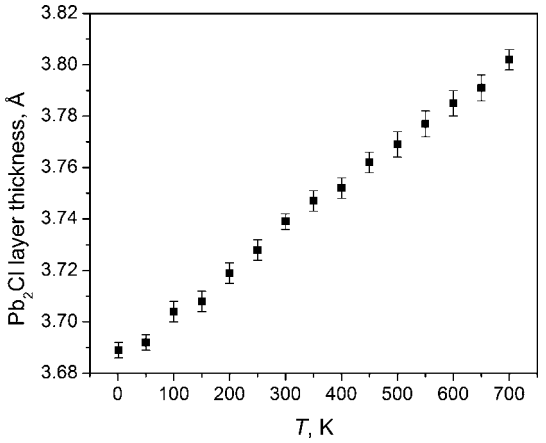

Figure 15. Temperature dependence of the Pb_2Cl slab thickness.

hematophanite structure, which contains only one octahedral layer, the angle of the rotation of the octahedra is larger (12.8° at 10 K and 10.3° at 650 K[14]) because of a larger strain.

Together with hematophanite $Pb_4Fe_3O_8Cl$, the new oxychlorides $Pb_4BiFe_4O_{11}Cl$ and $Pb_4Bi_2Fe_5O_{14}Cl$ can be considered as successive members of a perovskite-based homologous series with the general formula $A_{n+1}B_nO_{3n-1}Cl$ and n = 3−5, respectively. n corresponds to the number of BO_2 layers between the chlorine layers. The structure of the hypothetical member with n = 1 would be built of BO_2 planar squares sandwiched between the A_2Cl slabs. The member of the series with n = 2 is composed of BO_5 pyramidal layers connected through the apical O atoms and interleaved with A_2Cl slabs. This type of structure is indeed observed in the compounds $Pb_2BaCuFeO_5X$, where X = Cl and Br.[38] The structures of the successive members of the series can be obtained by introducing ABO_3 octahedral layers into the perovskite block (Figure 16). The structure of any member of the series can be illustrated as a stack of the following layers within one unit cell along the *c* axis:

$$-[Cl-A-BO_2-\{AO-BO_2\}_{n-1}-A-Cl]-$$

The structure of the hematophanite (n = 3) is very flexible. It can accommodate a number of different A (Pb, Ba, Sr) and B (Fe, Cu, Nb, Ta, Sb, Ru) cations, and substitution in the anion framework is also possible, e.g., Cl^- by Br^-.[30−35] The higher members of the series should possess a similar compositional

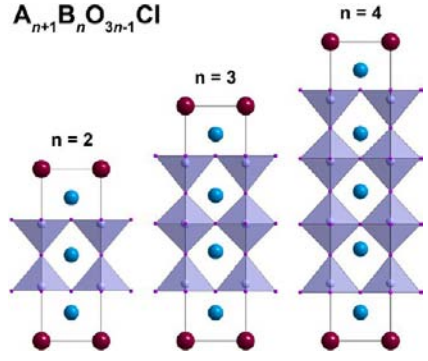

Figure 16. Idealized crystal structures of the first three members of the $A_{n+1}B_nO_{3n-1}Cl$ homologous series viewed along the $[100]_p$ direction. Experimental examples are $Pb_2BaCuFeO_5Cl$ (n = 2), $Pb_4Fe_3O_8Cl$ (n = 3), and $Pb_4BiFe_4O_{11}Cl$ (n = 4).

dx.doi.org/10.1021/ic302667a | Inorg. Chem. 2013, 52, 2208−2218

flexibility. However, the synthesis of pure compounds with high n may be complicated because layered structures with large layers are prone to stacking disorder.[39−43]

5. CONCLUSIONS

A new oxychloride $Pb_4BiFe_4O_{11}Cl$ was synthesized, and the temperature evolution of its crystal and magnetic structure was studied by a combination of TEM and NPD. The compound consists of $(Pb,Bi)_3Fe_4O_{11}$-truncated perovskite blocks separated by CsCl-like $(Pb,Bi)_2Cl$ slabs. $Pb_4BiFe_4O_{11}Cl$ orders antiferromagnetically below T_N = 595(17) K. It has a G-type AFM structure with the magnetic moments of the Fe atoms aligned perpendicularly to the c axis. The preparation of the $Pb_4BiFe_4O_{11}Cl$ compound enables us to propose the $A_{n+1}B_nO_{3n-1}Cl$ perovskite-based homologous series, with $Pb_4BiFe_4O_{11}Cl$ being its n = 4 member. The formation of the higher n = 5 member of this series is also confirmed.

■ ASSOCIATED CONTENT

Supporting Information

SXPD data, ED patterns at different temperatures, magnetization curve, electronic density of states, calculated ED patterns, and crystallographic data in CIF format. This material is available free of charge via the Internet at http://pubs.acs.org.

■ AUTHOR INFORMATION

Corresponding Author

*E-mail: Maria.Batuk@ua.ac.be. Tel: 00 32 32653695. Fax: 00 32 32653257.

Author Contributions

The manuscript was written through contributions of all authors. All authors have given approval to the final version of the manuscript.

Notes

The authors declare no competing financial interest.

■ ACKNOWLEDGMENTS

M.B. and D.B. thank Prof. Dr. Artem M. Abakumov for many helpful discussions and lots of advice. D.B. is thankful to Gerardo T. Martinez for his help with the STEM image simulation. M.B., D.B., and J.H. acknowledge funding from the Research Foundation—Flanders under Grant G.0184.09N. A.A.T. was supported by the Mobilitas grant of the ESF. The authors are grateful to the Paul Scherrer Institute (Switzerland) and ESRF for granting the beam time at HRPT and ID31, respectively. The experimental support of Denis Sheptyakov (PSI) and Andy Fitch (ESRF) is kindly acknowledged. M.G.R. and E.V.A. are thankful to the Russian Foundation for Basic Research (Grant 11-03-01257) and MSU-development program up to 2020. G.V.T. acknowledges funding from the European Research Council under the seventh Framework Program (FP7), ERC Grant 246791, COUNTATOMS. The authors acknowledge financial support from the Flemish Hercules 3 programme for large infrastructure.

■ REFERENCES

(1) Catalan, G.; Scott, J. F. *Adv. Mater.* **2009**, *21*, 2463−2485.
(2) Liu, Y. Y.; Vasudevan, R. K.; Pan, K.; Xie, S. H.; Liang, W.-I.; Kumar, A.; Jesse, S.; Chen, Y.-C.; Chu, Y.-H.; Nagarajan, V.; Kalinin, S. V; Li, J. Y. *Nanoscale* **2012**, *4*, 3175−3183.
(3) Khomskii, D. I. *J. Magn. Magn. Mater.* **2006**, *306*, 1−8.
(4) Seshadri, R.; Hill, N. A. *Chem. Mater.* **2001**, *13*, 2892−2899.
(5) Tsuchiya, T.; Saito, H.; Yoshida, M.; Katsumata, T.; Ohba, T.; Inaguma, Y.; Tsurui, T.; Shikano, M. *Mater. Res. Soc. Symp. Proc.* **2006**, *988*, 103.
(6) Batuk, D.; Hadermann, J.; Abakumov, A. M.; Vranken, T.; Hardy, A.; Van Bael, M.; Van Tendeloo, G. *Inorg. Chem.* **2011**, *50*, 4978−4986.
(7) Abakumov, A. M.; Hadermann, J.; Bals, S.; Nikolaev, I. V.; Antipov, E. V.; Van Tendeloo, G. *Angew. Chem., Int. Ed.* **2006**, *45*, 6697−6700.
(8) Hadermann, J.; Abakumov, A. M.; Nikolaev, I. V.; Antipov, E. V.; Van Tendeloo, G. *Solid State Sci.* **2008**, *10*, 382−389.
(9) Troyanchuk, I. O.; Kasper, N. V.; Mantytskaya, O. S.; Shapovalova, E. F. *Mater. Res. Bull.* **1995**, *30*, 421−425.
(10) Inaguma, Y.; Greneche, J.; Crosnier-Lopez, M.-P.; Katsumata, T.; Calage, Y.; Fourquet, J.-L. *Chem. Mater.* **2005**, *17*, 1386−1390.
(11) Rouse, R. C. *Am. Mineral.* **1971**, *56*, 625−627.
(12) Emery, J.; Cereze, A.; Varret, F. *J. Phys. Chem. Solids* **1980**, *41*, 1035−1040.
(13) Pannetier, J.; Batail, P. *J. Solid State Chem.* **1981**, *39*, 15−21.
(14) Knee, C. S.; Weller, M. T. *J. Mater. Chem.* **2001**, *11*, 2350−2357.
(15) Petricek, V.; Dusek, M.; Palatinus, L. *The crystallographic computing system JANA2006*; Institute of Physics: Praha, Czech Republic. 2006.
(16) Koch, C. *Determination of core structure periodicity and point defect density along dislocations*; Arizona State University: Phoenix, AZ, 2002.
(17) Koepernik, K.; Eschrig, H. *Phys. Rev. B* **1999**, *59*, 1743−1757.
(18) Andersen, O.; Pawlowska, Z.; Jepsen, O. *Phys. Rev. B* **1986**, *34*, 5253−5269.
(19) Perdew, J. P.; Wang, Y. *Phys. Rev. B* **1992**, *45*, 13244−13249.
(20) Spiel, C.; Blaha, P.; Schwarz, K. *Phys. Rev. B* **2009**, *79*, 115123.
(21) Wojdyr, M. *J. Appl. Crystallogr.* **2010**, *43*, 1126−1128.
(22) Van Smaalen, S. *Incommensurate Crystallography*; Oxford University Press: Oxford, U.K., 2007; p 284.
(23) Campbell, B. J.; Stokes, H. T.; Tanner, D. E.; Hatch, D. M. *J. Appl. Crystallogr.* **2006**, *39*, 607−614.
(24) Findlay, S. D.; Shibata, N.; Sawada, H.; Okunishi, E.; Kondo, Y.; Ikuhara, Y. *Ultramicroscopy* **2010**, *110*, 903−923.
(25) Momma, K.; Izumi, F. *J. Appl. Crystallogr.* **2011**, *44*, 1272−1276.
(26) Gillberg, M. *Ark. Mineral. Geol.* **1960**, *2*, 565−570.
(27) Brown, I. D.; Altermatt, D. *Acta Crystallogr., Sect. B: Struct. Sci.* **1985**, *41*, 244−247.
(28) Wills, A. S. *VaList*, program available from www.ccp14.ac.uk.
(29) Perez-Mato, J. M.; Zakhour-Nakhl, M.; Weill, F.; Darriet, J. *J. Mater. Chem.* **1999**, *9*, 2795−2807.
(30) Li, R. *Phys. C (Amsterdam, Neth.)* **1997**, *277*, 252−256.
(31) Li, R. *J. Solid State Chem.* **1997**, *130*, 154−156.
(32) Crooks, R. J.; Knee, C. S.; Weller, M. T. *Chem. Mater.* **1998**, *10*, 4169−4172.
(33) Mclaughlin, A. C.; McAllister, J. A.; Stout, L. D.; Attfield, J. P. *Solid State Sci.* **2002**, *4*, 431−436.
(34) Cava, R. J.; Bordet, P.; Capponi, J. J.; Chaillout, C.; Chenavas, J.; Fournier, T.; Hewat, E. A.; Hodeau, J. L.; Levy, J. P.; Marezio, M.; Batlogg, B.; Rupp, L. W. *Phys. C (Amsterdam, Neth.)* **1990**, *167*, 67−74.
(35) Hyatt, N. C.; Hriljac, J. A. *Phys. C (Amsterdam, Neth.)* **2002**, *366*, 283−290.
(36) Dachraoui, W.; Hadermann, J.; Abakumov, A. M.; Tsirlin, A. A.; Batuk, D.; Glazyrin, K.; McCammon, C.; Dubrovinsky, L.; Van Tendeloo, G. *Chem. Mater.* **2012**, *24*, 1378−1385.
(37) Abakumov, A. M.; Batuk, D.; Hadermann, J.; Rozova, M. G.; Sheptyakov, D. V.; Tsirlin, A. A.; Niermann, D.; Waschkowski, F.; Hemberger, J.; Van Tendeloo, G.; Antipov, E. V. *Chem. Mater.* **2011**, *23*, 255−265.
(38) Li, R. *Inorg. Chem.* **1997**, *36*, 4895−4896.
(39) Whaley, L. W.; Lobanov, M. V.; Sheptyakov, D.; Croft, M.; Ramanujachary, K. V.; Lofland, S.; Stephens, P. W.; Her, J.; Van Tendeloo, G.; Rossell, M.; Greenblatt, M. *Chem. Mater.* **2006**, *18*, 3448−3457.

(40) Hungria, T.; MacLaren, I.; Fuess, H.; Galy, J.; Castro, A. *Mater. Lett.* **2008**, *62*, 3095−3098.
(41) Abakumov, A. M.; Hadermann, J.; Batuk, M.; D'Hondt, H.; Tyablikov, O. A.; Rozova, M. G.; Pokholok, K. V.; Filimonov, D. S.; Sheptyakov, D. V.; Tsirlin, A. A.; Niermann, D.; Hemberger, J.; Van Tendeloo, G.; Antipov, E. V. *Inorg. Chem.* **2010**, *49*, 9508−9516.
(42) Korneychik, O. E.; Batuk, M.; Abakumov, A. M.; Hadermann, J.; Rozova, M. G.; Sheptyakov, D. V.; Pokholok, K. V.; Filimonov, D. S.; Antipov, E. V. *J. Solid State Chem.* **2011**, *184*, 3150−3157.
(43) Wang, Y.; Yu, R. *Phys. Status Solidi A* **2009**, *206*, 31−35.